Geophysical Journal International

Geophys. J. Int. (2009) **179,** 1265–1278 doi: 10.1111/j.1365-246X.2009.04187.x

Thermal constraints on the frictional conditions of the nucleation and rupture area of the 1992 Nicaragua tsunami earthquake

Martin Heesemann,[1]* Ingo Grevemeyer[2] and Heinrich Villinger[1]

[1]*Department of Geosciences, University of Bremen, Bremen, Germany. E-mail: heesema@uni-bremen.de*
[2]*IFM-GEOMAR, Leibniz-Institute of Marine Sciences, Kiel, Germany*

Accepted 2009 March 18. Received 2009 March 14; in original form 2008 July 1

SUMMARY

The 1992 Nicaragua earthquake was a 'tsunami earthquake', which generated tsunamis disproportionately large for its surface wave magnitude $M_s = 7.2$. Seismological studies and tsunami simulation indicated that the event was a slow earthquake, which occurred on the plate boundary between the subducting Cocos plate and the overriding Caribbean plate. We present a finite element model that enables us to estimate for the first time the temperature and inferred frictional conditions in the rupture area of a tsunami earthquake. Direct and indirect observations are used to constrain all model parameters, and surface heat-flux measurements provide independent information to verify the model results. Furthermore, we used a genetic algorithm to perform a sensitivity analysis of all model parameters and to define the spatial range of thermally defined updip limit of the seismogenic zone. The earthquake nucleated in the seismogenic zone at temperatures of ∼150 °C and propagated updip towards the trench axis. The centroid or centre of mass of moment release was located in a region characterized by temperatures of ∼50 °C. Thus, the rupture propagated through a region where plate motion is normally accommodated by aseismic creep. Our observations support a model in which tsunami earthquakes nucleate in the seismogenic zone near its updip limit. However, in such an environment coupled asperities are perhaps too small to cause large earthquakes. Seamounts, however, are abundant on the incoming Cocos plate. Therefore, in addition to temperature-dependent metamorphic induration of sediments, increased normal stress by seamount subduction may contribute to accumulate stress sufficiently large to release enough energy near the updip limit of the seismogenic zone to promote dynamic slip along a normally aseismic décollement all way to the ocean.

Key words: Numerical solutions; Heat flow; Seismicity and tectonics; Subduction zone processes; Heat generation and transport.

1 INTRODUCTION

Any great shallow subduction zone earthquake is expected to be followed by a substantial tsunami caused by the large displacement of water near the seafloor. However, a subclass of events called tsunami earthquakes excites considerably larger tsunamis than expected from its seismic magnitude (Kanamori 1972). For instance, although they were much smaller in seismic moment magnitude (M_w), the tsunamis generated by two historic tsunami earthquakes, the 1946 Aleutian earthquake ($M_w = 8.2$) and the 1896 Sanriku earthquake ($M_w = 8.0$), produced devastating tsunamis of similar magnitudes as the 1960 Chile ($M_w = 9.6$), the 1964 Alaska ($M_w = 9.2$) and the 2004 Sumatra ($M_w > 9$) earthquakes (Geist 2002; Geist *et al.* 2006).

Because of the discrepancy between seismic and tsunami magnitude, tsunami earthquakes are particularly dangerous. The 1896 Sanriku earthquake, for example, was felt only moderately along the Japanese coast, but very large tsunamis hit the coast *ca.* 30 min later and drowned more than 22 000 people. Due to the absence of strong ground motion, people did not evacuate to safe areas. Consequently, for disaster mitigation, it is particularly important to understand the processes governing tsunamigenic earthquakes.

To study tsunami earthquakes, the 1992 Nicaragua event is particularly well suited since it is the largest tsunami earthquake ($M_w = 7.7$, $M_t = 7.9$) ever recorded by global seismic broad-band networks (Kanamori & Kikuchi 1993; Satake & Tanioka 1999). Digital data have been a treasure trove for detailed studies of seismic body waves, surface waves and tsunami simulation to calculate the nucleation and rupture history of the slow earthquake (Ide *et al.* 1993; Satake 1994; Velasco *et al.* 1994; Ihmle 1996a). Moreover, the convergent margin off Nicaragua and Costa Rica is well studied, for example, by numerous deep sea drilling sites, active and

*Now at: Pacific Geoscience Centre, Geological Survey of Canada, Sidney, British Columbia, V8L 4B2, Canada. E-mail: Martin.Heeseman@nrcan.gc.ca

passive seismic surveys, surface heat-flux measurements, and GPS installations.

Compared to other thrust earthquakes, tsunami earthquakes usually have a longer source time function, and a slower and smoother rupture. Seismic body waveform inversions of tsunami earthquakes indicate shallow dipping thrust fault mechanisms (dip angle ∼6–10°), occurring at shallow depth (<15–20 km) near the trench axis and seaward of most other thrust zone events (Pelayo & Wiens 1992). Overall, these observations suggest that the slow rupture results from seismic slip along a weak basal décollement cutting through shallow sedimentary rocks (Pelayo & Wiens 1992). Due to the low rigidity of these sedimentary rocks, shallow thrust faulting will cause larger seismic slip and hence increase tsunami amplitudes (Geist & Bilek 2001).

In contrast to tsunami earthquakes, the rupture zones of regular subduction thrust earthquakes, which are caused by stick-slip frictional instabilities (Scholz 1998), are usually confined to greater depths. Byrne *et al.* (1988) suggested that unconsolidated sediments in the upper part of the subduction thrust cause stable sliding and hence prevent earthquake nucleation and rupture propagation. Accordingly, they postulated that the updip limit of the seismogenic zone occurs at the transition from the sedimentary accretionary prism to the backstop of competent continental rock. The updip limit is, however, mostly found seaward of the backstop and its location has been correlated with modelled subduction thrust temperatures between 100 and 150 °C (Hyndman & Wang 1993; Hyndman *et al.* 1995; Oleskevich *et al.* 1999), later on. Yet, the correlation of the updip limit of the seismogenic zone with temperature is not well understood. Many diagenetic and low-grade metamorphic processes that cause induration of subducting sediments and increased effective stress at temperatures between 70 and 150 °C have been identified, but in general no single process seems to dominate (e.g. Moore & Saffer 2001).

In order to cause slip along the shallow normally aseismic basal décollement, tsunami earthquakes may nucleate in the seismogenic zone below the updip limit with enough energy to dynamically propagate updip (Scholz 1998; Seno 2002). Alternatively, they may nucleate at shallow non-sedimentary asperities where seamounts or abyssal hills cause contact zones with the overriding plate (Polet & Kanamori 2000; Bilek & Lay 2002).

We developed a thermal finite element (FE) model to yield the thermal state of the coupling zone and hence to constrain the thermally defined updip limit of the rupture area. First, we used the reported results of seismic and GPS surveys to constrain the model geometry. Second, model parameters were derived from physical properties measured at several Ocean Drilling Program (ODP) drill sites, previously reported seafloor heat-flux data, and the sediment distribution on the subducting oceanic crust. Finally, new heat-flux data, measured on the continental slope off Nicaragua, provided independent constraints for a genetic algorithm (GA), which we used to find model parameters in agreement with our data and to estimate the uncertainties in the computed thermal state of the rupture zone.

2 THE 1992 NICARAGUA EARTHQUAKE

The 1992 September 2 Nicaragua earthquake, which originated at the coupling zone between the subduction Cocos Plate and the overriding Caribbean Plate (*cf.* Fig. 1), generated tsunamis that caused extensive damage on the Pacific coast of Nicaragua despite its moderate seismic surface wave magnitude of $M_s = 7.2$. Field surveys for seismic intensity and tsunami run-up height showed that the seismic intensity was small (III of the Modified Mercalli scale), but the tsunami run-up was ∼10 m above mean sea level (Baptisa *et al.* 1993; Satake *et al.* 1993) and caused at least 170 causalities.

The epicentre of the 1992 Nicaragua event, computed by the National Earthquake Information Center (NEIC), using short-period teleseismic data, is located near the shelf break, approximately 65–70 km from the trench axis (red star Figs 1 and 6). Seismic body waveform inversion indicates a thrust faulting mechanism with a dip of 14–15° and a depth of ∼21 km (Ide *et al.* 1993). This corresponds roughly to the depth and dip of the plate interface as derived from reflection and refraction seismic data (Ranero *et al.* 2000; Walther *et al.* 2000). Due to the long duration and slow rupture velocity of the earthquake, seismologists observed differences of 45–52 s between the centroid time and the NEIC origin time (Ide *et al.* 1993; Kanamori & Kikuchi 1993). Centroids represent the centre of mass of moment release and are calculated from long-period surface waves. While short-period data indicates the nucleation area of the tsunami event, long-period data can be used to study the propagation of seismic slip. Ihmle (1996a) studied different wave bands and found that with decreasing frequencies centroids move towards the trench. The centre of lowest frequency radiation is situated closest to the trench, about 40 km seaward of the NEIC epicentres, while intermediate frequencies centroids range between low frequency centroids and the epicentre (Fig. 1b). Spectral inversion of long-period Rayleigh and Love waves (157–288 s) yield similar results, indicating a centroid location 54 km SW of the NEIC epicentre, at <10 km depth, with a fault zone dipping at ∼6° (blue star Figs 1 and 6), and a predominant rupture azimuth of 140° (Velasco *et al.* 1994). The shallow depth and low dip angle correspond roughly to the geometry of the plate interface updip from the NEIC epicentres and supports rupture propagation towards the trench (Fig. 2). Tsunami simulation supports the fact that rupture reached into the trench (Satake 1994; Bilek & Lay 2002).

Most aftershocks occur in a 40-km-wide zone parallel to the trench (Fig. 1), which stretches 100 km to the NW and 150 km to the SE of the epicentre (Ihmle 1996a). Only a few events occurred seaward of the epicentre near the trench axis and available Harvard centroid moment tensor (CMT) solutions indicate normal faulting mechanisms. Thus, earthquakes near the trench axis may represent intraplate events being related to bending of the subducting lithosphere rather than being related to earthquake processes in the subduction thrust. Nevertheless, large interplate earthquakes may affect the regional stress field and may therefore trigger intraplate earthquakes (Christensen & Ruff 1983). Harvard CMT solutions of aftershocks further landward indicate thrust-faulting mechanisms. In contrast to the main shock, the aftershock distribution suggests that most events ruptured downdip. It is important to note that the location of the aftershocks correspond well with the seismic front (Byrne *et al.* 1988; Newman *et al.* 2002), which marks the updip limit of the seismogenic zone. Byrne *et al.* (1988) suggest that the shallow subduction thrust seaward of the seismic front is velocity strengthening. Therefore, the main shock propagated into a regime expected to be characterized by stable sliding (Scholz 1998) and hence slip occurred along a normally aseismic and weak décollement.

3 THE NUMERICAL MODEL

To constrain the thermal updip limit of the seismogenic zone, we study the temperature of the décollement zone using a steady state FE model, which is based on the Comsol Multiphysics® toolbox, and Matlab®. The geometry of the FE model (Fig. 2) is derived

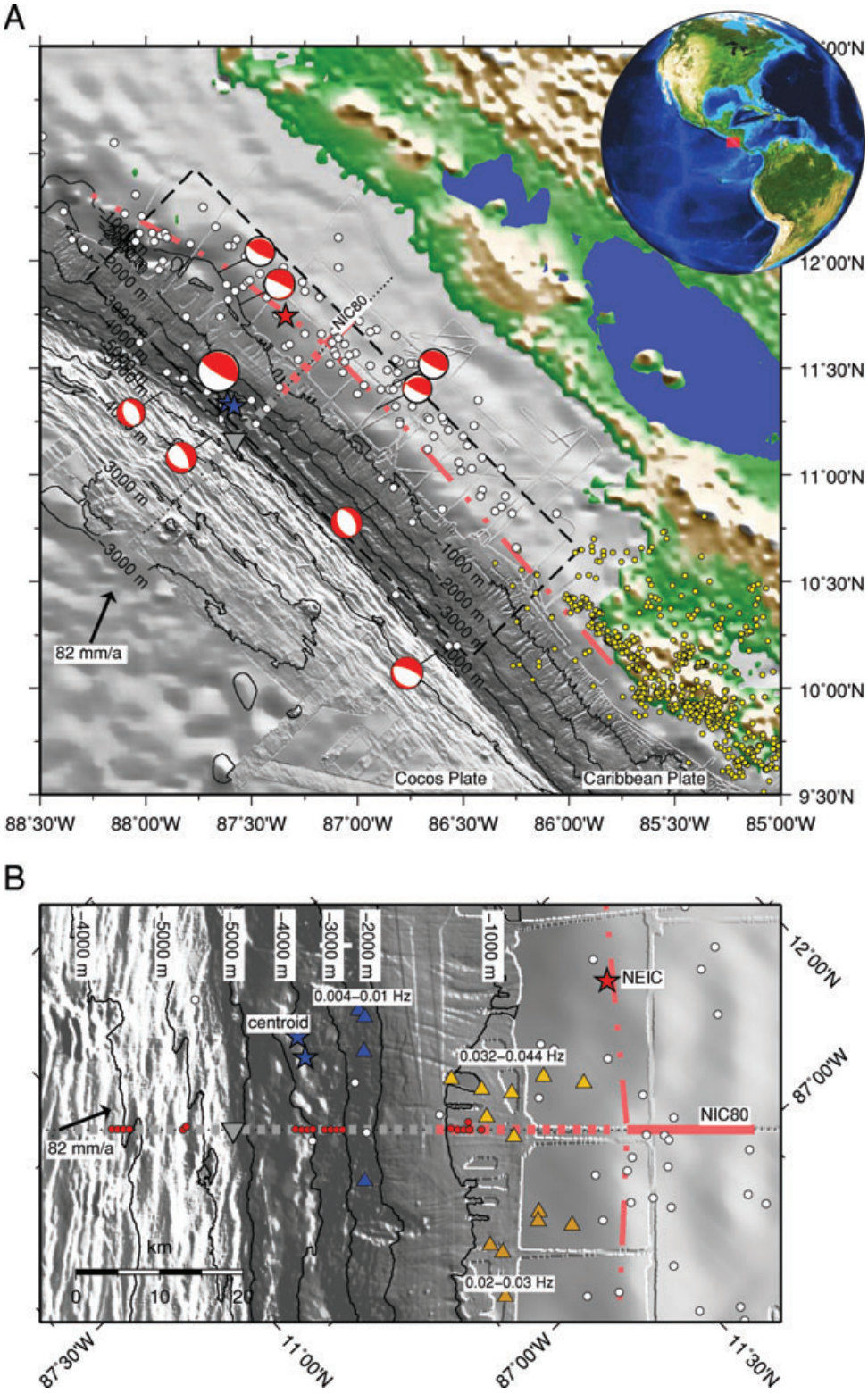

Figure 1. Artificially illuminated seafloor relief in the area of the 1992 Nicaragua tsunami event. The red star is the NEIC epicentre, indicating the area where the rupture started. Blue stars are centroids (Velasco *et al.* 1994; Newman *et al.* 2002). The aftershocks (white circles) relocated by Ihmle (1996a) occurred in a 3-month period following the main event. The first part of model transect (NIC80) is marked by dashed grey line. At model temperatures >100 °C the line turns red and model temperatures >150 °C are marked by a solid red line. The 150 °C isotherm is extrapolated to both sides of the transect. (a) The moment release within the slip area (boxed region; Ihmle 1996b) was used for tsunami simulation (Geist & Bilek 2001). Harvard CMT solutions, which have been assigned to relocated events, are shown for the main shock and largest aftershocks. Yellow dots are earthquakes relocated by (Newman *et al.* 2002). (b) The triangles are spatial centroids (Ihmle 1996a), illustrating the slow rupture process; with decreasing frequency spatial centroids moved further trenchward. Small red dots on the seismic profile (Walther *et al.* 2000) mark locations where heat-flux measurements were obtained during the RV Meteor cruise M54-2. The arrow illustrates the velocity of the Cocos Plate with respect to the Caribbean Plate.

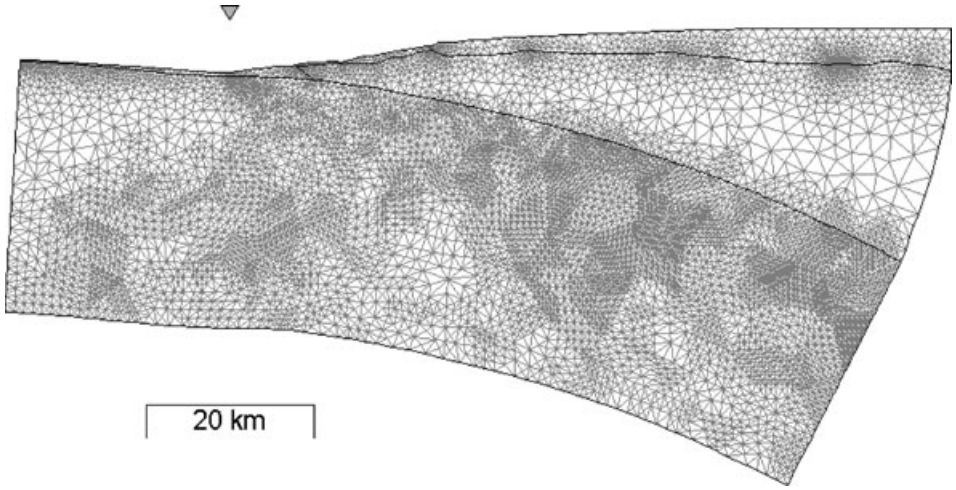

Figure 2. Complete geometry and mesh of the FEM model. The mesh, shown without vertical exaggeration, consists of 20 289 triangular elements and has 40 914 degrees of freedom. The triangle above the geometry marks the location of the deformation front.

from time migrated and depth converted reflection seismic data, using velocities from focusing analysis (Ranero *et al.* 2000) and seismic refraction work (Walther *et al.* 2000). These data indicate two different main units building the continental margin: slope sediments and an underlying basement consisting of oceanic igneous rocks. Therefore, the model geometry is divided into three domains: a sedimentary layer (Seds), the continental basement (CnBs) and the subducting oceanic crust (OcCr).

The upper boundaries of the domains are approximated by cubic B-splines using a modified version of the 'splinefit' script implemented by Nielsen (2005). B-splines offer a high level of flexibility during geometry assembly and avoid geometric singularities at the same time, by ensuring smooth boundaries (existence of continuous second derivative). Then, a method described by Romani & Sabin (2004) is used to transform the B-splines into an equivalent series of cubic Bézier curves that can directly be handled by Comsol Multiphysics®. See Fig. 2 for an illustration of the complete meshed geometry with 40 914 degrees of freedom, and 20 289 triangular elements.

The 2-D model is based on the non-conservative steady state heat conduction and advection equation

$$\nabla \cdot (-k\ \nabla T) = Q - \rho c_p\ \mathbf{v} \cdot \nabla T \tag{1}$$

which assumes incompressible flow and ensures that no unphysical source term arises from a flow field where the incompressibility constraint is not absolutely fulfilled (Comsol 2005, pp. 162). Hence, the temperature distribution in the model domains depends not only on the geometry but also on the boundary conditions at the edges of the domains, the thermal conductivity (k), the volumetric heat capacity (ρc_p), the heat production (Q) and the velocity ($\mathbf{v}$) determining the advective heat transport.

3.1 Parameter constraints

Since all model parameters interact and influence the temperature distribution at the décollement, it is important to constrain them as good as possible by direct and indirect observations. Defining the velocity field, we assume that the Cocos Plate subducts beneath a stationary Caribbean Plate and computed a convergence rate of 82 mm a^{-1}, using the Plate Motion Calculator (UNAVCO 2006) and the corresponding rotation pole published by DeMets (2001). Accordingly, the OcCr is the only domain with advective heat transport and the magnitude of its velocity (78 mm a^{-1}) is given by plate velocity component that is parallel to the model transect (*cf.* Fig. 1b). The direction of the modelled velocity field is parallel to the upper boundary of the oceanic crust.

The thermal properties and the boundary conditions of the OcCr domain are based on global models of oceanic crust cooling histories evaluated by Stein & Stein (1992). We chose the half-space cooling model

$$T(t,\ z) = (T_i - T_{sf})\mathrm{erf}\left(\frac{z}{2\sqrt{\kappa\ t}}\right) \tag{2}$$

with

$$\kappa = k/(\rho c_p)$$

to prescribe the temperature field at the seaward and lower boundaries of the 24 Ma old (Barckhausen *et al.* 2001) subducting oceanic crust. Following values for the model parameters were reported by Stein & Stein (1992): $k = 3.138$ W (m K)$^{-1}$, $c_p = 1.171$ kJ (kg K)$^{-1}$ and $\rho = 3330$ kg m^{-3}. Furthermore, no heat production in the OcCr domain, and an initial crust temperature T_i of 1450 °C and a constant seafloor temperature T_sf of 0 °C are assumed.

We adopted these parameter values, constrained by global heat flux and bathymetry data (Stein & Stein 1992), except for the temperature of the upper oceanic crust. Harris & Wang (2002) found that it is important to modify this simple half-space cooling model to account for advective cooling of the upper oceanic crust by circulating sea water. This is especially important in models that are designed to investigate the frontal part of the subduction zone including the updip limit of the seismogenic zone. Having a closer look at the oceanic crust–sea water interface, there are two facts that deviate from the assumption of a constant temperature of 0 °C. First, we observed bottom water temperatures of 2 °C during our heat-flux measurements. Second, the oceanic crust is not in direct contact with the water column but insulated with a blanket of sediments and cooled by fluid advection beneath the cover at the same time. To account for the first observation, one can add 2 °C to all temperatures in the model. To include the second observation, we calculated the temperature difference between bottom water and oceanic crust–sediment interface (ΔT), assuming the heat transfer in the sediments to be purely conductive, by using Fourier's law of

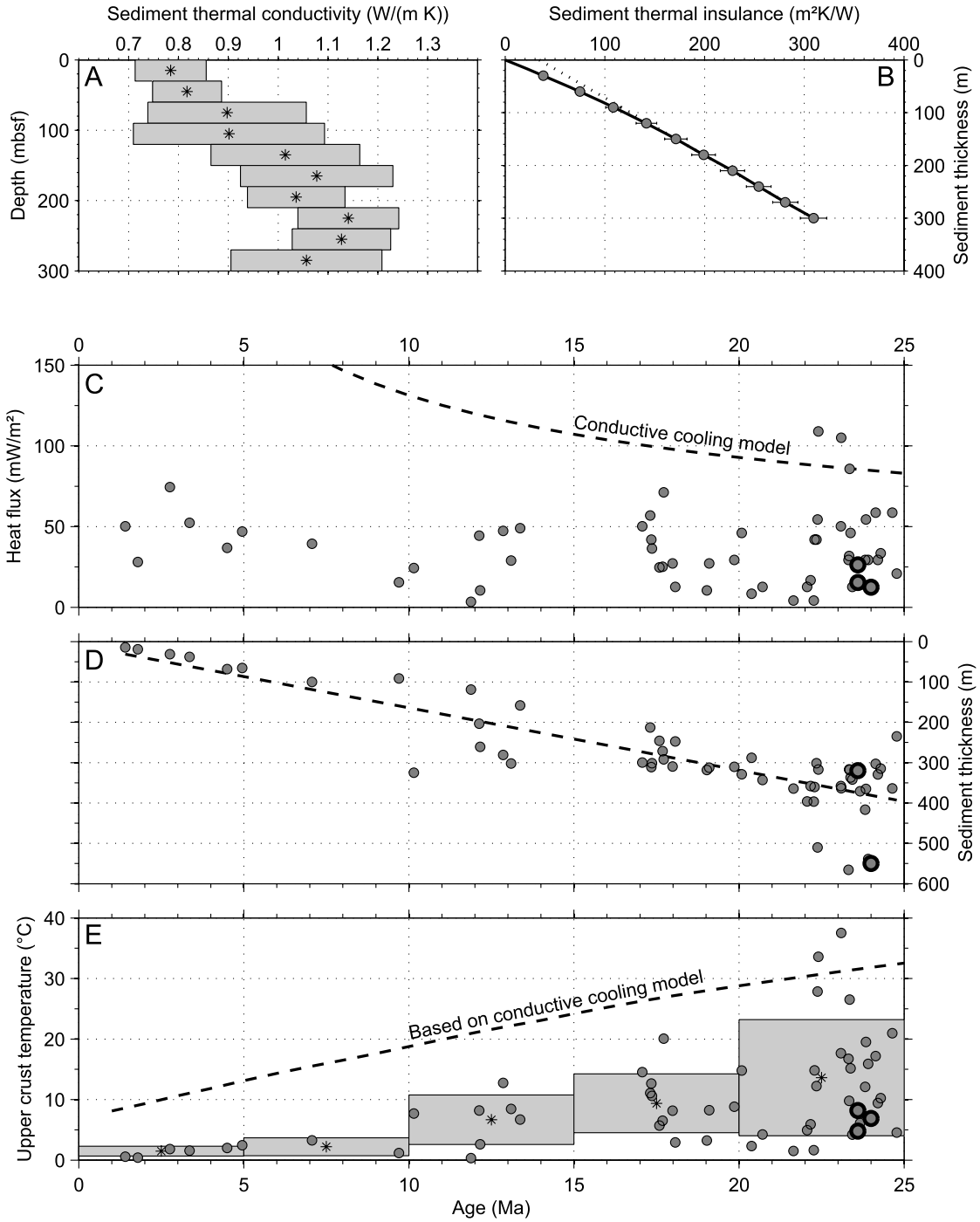

Figure 3. (a) Mean (stars) and standard deviation (boxes) of thermal conductivities measured in sedimentary sections of ODP Sites 844, 845 (Mayer *et al.* 1992), and 1256 (Wilson *et al.* 2003). (b) Mean thermal insulance of the sedimentary column at the ODP Sites. Errors are derived from standard deviation of thermal conductivities. The fit of dotted line is used for linear extrapolation of the thermal insulation to greater sediment thicknesses. (c) Heat-flux measurements on the subducting Cocos Plate, reported by Pollack *et al.* (1992) (plain symbols) and Grevemeyer *et al.* (2005) (bold symbols), versus the crustal age (Barckhausen *et al.* 2001). (d) Thickness of sediment cover at the locations of the heat-flux measurements. If not otherwise available the sediment cover is interpolated using global data published by Divins (2005). (e) Temperatures at the sediment-basement interface (filled symbols) are the product of the conductive surface heat flux (c) and the thermal insulance of the sedimentary column (b) with the thickness (d) at the specific location. Stars and boxes show the binned mean values and standard deviations of the upper crust temperatures. The dashed line represents the temperatures that would results from a conductive cooling model (c) and a linearly increasing sedimentary column (d).

conduction

$$q = k\,\Delta T/\Delta z \iff \Delta T = q\,I. \tag{3}$$

Here, k is the thermal conductivity, Δz the thickness of the sediments, q the surface heat-flux and I the thermal insulance, the quotient of Δz and k. The depth dependency of I (Fig. 3b) was computed based on the geometric mean thermal conductivities (Fig. 3a) of sediments covering the subducting oceanic crust segment. The thermal

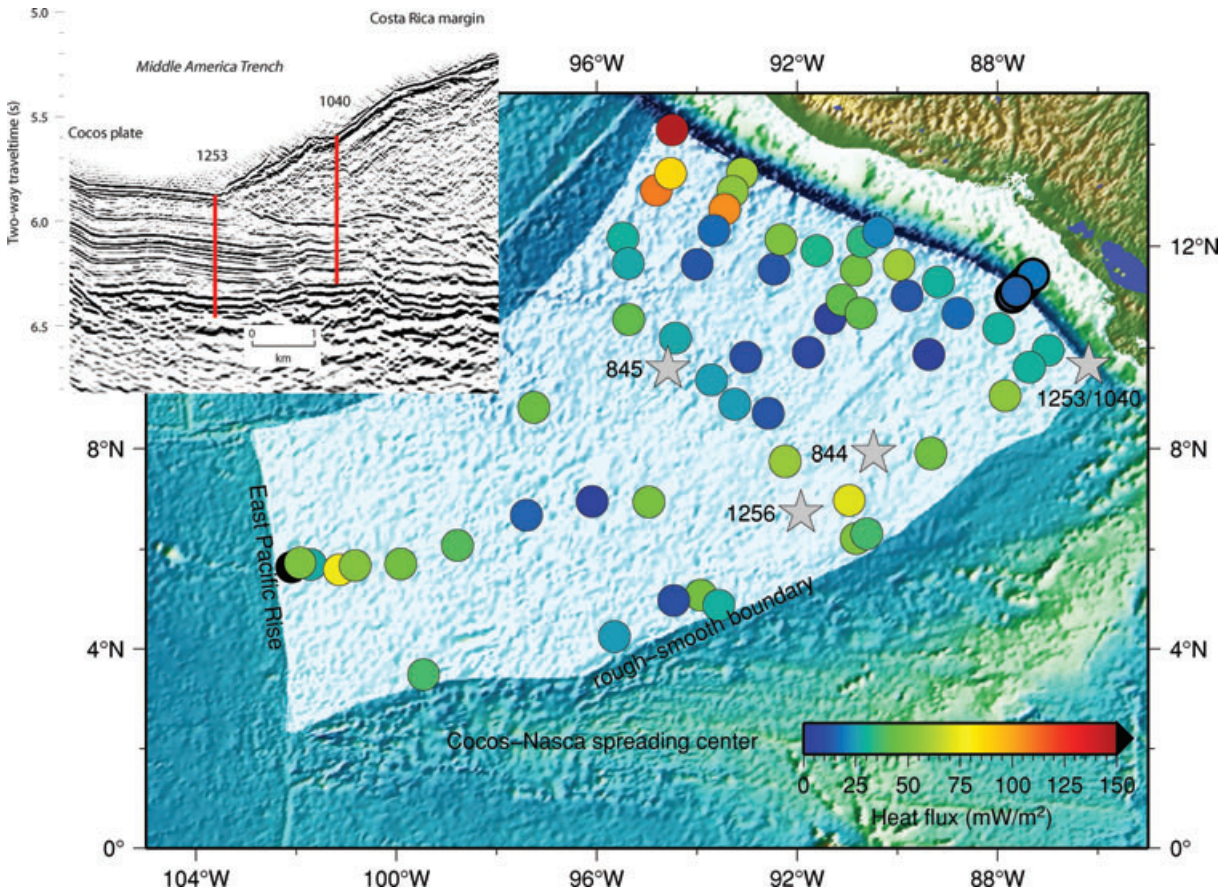

Figure 4. Locations of ODP Sites and seafloor heat-flux measurements over elevation model (NGDC 2005). Inset shows detailed locations of ODP Sites 1253 and 1040 off Costa Rica. The oceanic crust segment that originates from the East Pacific Rise and subducts off Nicaragua is highlighted.

conductivities were measured on split cores from ODP Sites 844, 845 (Mayer *et al.* 1992) and 1256 (Wilson *et al.* 2003), the locations of which are shown in Fig. 4. Along with abundant heat-flux data from (Vaquier *et al.* 1967; Sclater *et al.* 1970; Langseth *et al.* 1971; Bookman *et al.* 1972) that is included in the global heat-flux compilation of Pollack *et al.* (1992) (Fig. 3c), and sediment thickness data (Fig. 3d) published by Divins (2005), the local thermal insulance was used to compute temperatures at the sediment–basement interface (Fig. 3d), assuming a constant bottom water temperature of 0 °C.

Estimated averages over time of the computed temperatures are used to prescribe the temperature of the upper OcCr boundary until it reaches the deformation front. Past the deformation front, a continuous boundary condition is applied, assuming the ceasing of advective circulation in the upper oceanic crust when it is subducted. Note that in the model surface heat flux values seaward of the deformation front are used as boundary conditions and cannot be used to verify the model by comparison to field measurements.

The thermal properties of the Seds and CnBs domains are derived from measurements at three ODP Sites (Fig. 5). Thermal conductivities were directly measured on cored material whereas the rate of radiogenic heat production (Q_r) is computed using downhole logging data and the empiric equation

$$Q_\mathrm{r}\,[\mu\mathrm{W/m^3}] = 10^{-5}\rho(9.51c_\mathrm{U} + 2.56c_\mathrm{Th} + 3.48c_\mathrm{K}).$$

Here, ρ is the rock density (kg m^{-3}), c_U (ppm), c_{Th} (ppm) and c_K (wt per cent) are radioactive-element contents (Buecker & Rybach 1996; Grevemeyer *et al.* 2003). Density data is provided by the Hostile Environment Lithodensity Tool (HLDT), and the contents of the radioactive-elements were measured using the Natural Gamma Ray Spectrometry Tool (NGT).

In the data, the Seds domain is represented by a ∼150 m thick section of slope sediments which is probed ∼1 km landwards of the Middle America Trench off Costa Rica at ODP Site 1040 (Kimura *et al.* 1997) (*cf.* inset Fig. 4). The CnBs domain, which presumably consists of oceanic igneous rocks, is represented by two ∼70- and ∼390-m-thick sections of oceanic basement penetrated at ODP Sites 1253 (Morris *et al.* 2003) and 1256 (Wilson *et al.* 2003), respectively. The oceanic rocks at Site 1253 are recovered from two different intervals: a 30-m-thick upper igneous unit (gabbro sill), and a 40-m-thick lower igneous, separated by a 30-m-thick sedimentary unit.

3.2 Initial model

We used the parameter constraints, derived in the previous section and summarized in Figs 3 and 5, to define a set of parameters for an initial model and a constraining range for each model parameter both shown in Table 1. Surprisingly, all values of our initial model parameters are notably lower than used by other authors in similar models. As an example, the parameters used by Harris & Wang (2002) for a thermal model of the subduction zone off Nicoya Peninsula, Costa Rica, are listed in Table 1. Measured surface heat flux values on the subduction plate are exceptionally low (Langseth & Silver 1996), signalling low upper oceanic crust temperatures, and new measurements on our modelled transect are even below the regional

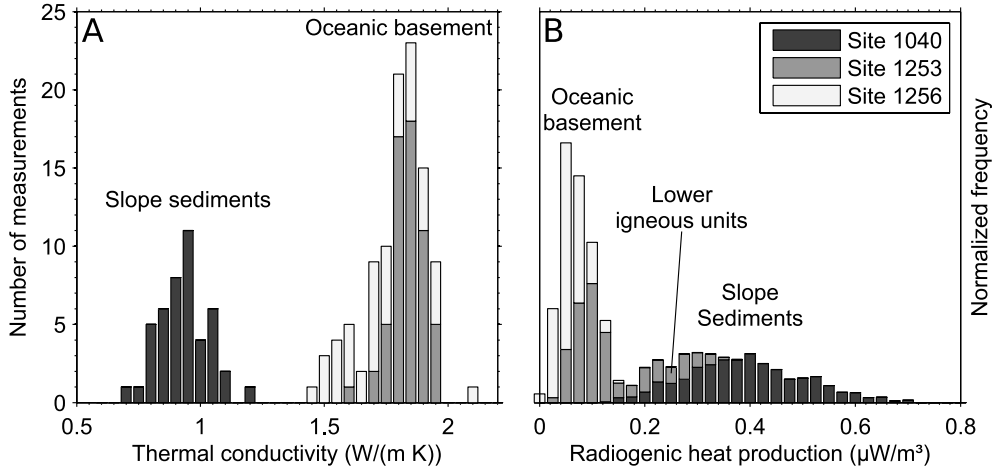

Figure 5. Thermal conductivies measured on core-samples (a) and radiogenic heat production derived from downhole logging data (b) at three ODP Sites (*cf.* Fig. 4).

Table 1. Parameters and results of selected models.

Domain	Variable parameters					Results			References
	OcCr	CnBs		Seds					
	T_{in}(°C)	k [W (m K)$^{-1}$]	Q (μ W m^{-3})	k [W (m K)$^{-1}$]	Q (μ W m^{-3})	$x_{100°C}$ (km)	$x_{150°C}$ (km)	Misfit (mW m^{-2})	ID #
Constraints	0–20	1.8–2.2	0–0.4	0.8–1.2	0.2–0.8	(30.0–38.5)	(60.7–73.9)	0–2.5	
Initial model	7.0	1.90	0.1	1.00	0.4	35.0	68.0	2.1	1
Best model	10.0	1.90	0.1	1.15	0.5	34.6	68.4	1.2	1986
Shallow model	18.0	1.80	0.3	0.90	0.5	30.0	60.7	1.6	534
Deep model	0.0	2.15	0.1	1.00	0.4	38.5	73.9	1.9	1173
GA range	0–40	0.6–3	0–2.5	0.6–3	0–2.5	(16.3–45.6)	(39.3–79.7)	(0.9–21.5)	
Best fit	21.5	1.60	0.2	1.80	0.0	31.3	62.8	0.9	3795
Harris & Wang	7.0	2.70	1.5	1.20	0.6	35.5	62.2	7.9	2039

Notes: Numbers in parentheses in the highlighted lines result from the other given ranges. All misfit values, except for the Harris & Wang (2002) model, are in respect to the scenario with low BSR derived heat-flux values.

average (see Fig. 3). Moreover, average sediment thermal conductivies below 1 W (m K)$^{-1}$ are lower than usually found in ODP boreholes, and finally the thermal conductivity and radiogenic heat production values of the igneous oceanic rocks that are believed to build the continental basement are much lower than found in usual continental basement. Therefore, parameter values for the CnBs domain often used by other authors are beyond of our constrained range. To verify the chosen parameters, we compared surface heat-flux values computed with our initial parameter set (Fig. 6a), as well as with the parameters used by Harris & Wang (2002) (Fig. 6b), to new heat-flux data from the continental slope.

During RV Meteor cruise M54-2 in summer 2002, we obtained 25 surface heat-flux measurements on the continental slope off Nicaragua (Grevemeyer *et al.* 2005). 15 of these measurements are located on our modelled transect, the seismic multichannel line NIC80, shot with a 6 km streamer in 2000 by the University of Texas at Austin. Two different heat-flux probes of violin bow design (Hyndman *et al.* 1979) were used to acquire the data. The instruments have 11 and 22 thermistors, which are spaced in 0.27 m intervals and mounted inside an oil filled hydraulic tube that penetrates into a sedimented seafloor. Thus, the probes are able to obtain thermal gradients over a length of 3 and 6 m, respectively. Both probes are equipped with on-line data transmission for operation control and independent data storage inside the instrument for double data security. During every other probe penetration, *in situ* thermal conductivity measurements were made by applying a 20 s pulse of electric current along heater wires within the tubing. The recorded temperature decays caused by this calibrated heat pulse allow to estimate the thermal conductivities of the sediments surrounding temperature sensor (Hartmann & Villinger 2002).

In addition to measurements with the heat-flux probes, thermal gradients were measured by autonomous temperature loggers (Pfender & Villinger 2002) mounted on gravity corers. Thermal conductivities from the recovered core material have been measured using needle probes (von Herzen & Maxwell 1959), which were inserted into undisturbed areas of split cores. After penetration into the sedimented seabed, the sensors record a pulse of frictional heating which decays while the tools remains in the seafloor for 7–10 min. Then, temperatures and thermal conductivity measurements are jointly inverted to obtain the surface heat flux. Individual heat flux values and the number of temperature measurements used to derive the thermal gradients are published in Grevemeyer *et al.* (2005).

In addition to the measured heat flux data, we calculated seafloor heat flux values from bottom simulating reflectors (BSR), which were imaged on the middle part of the slope off Nicaragua. Due to the uncertainties in the absolute magnitude of the BSR-derived heat flux values, we used the procedure described by Grevemeyer & Villinger (2001) to calibrate the data with heat flux probe measurements at the same location. Unfortunately, this calibration is ambiguous since our relevant heat-flux probe measurements, located ∼40 km landward from the deformation front, can be

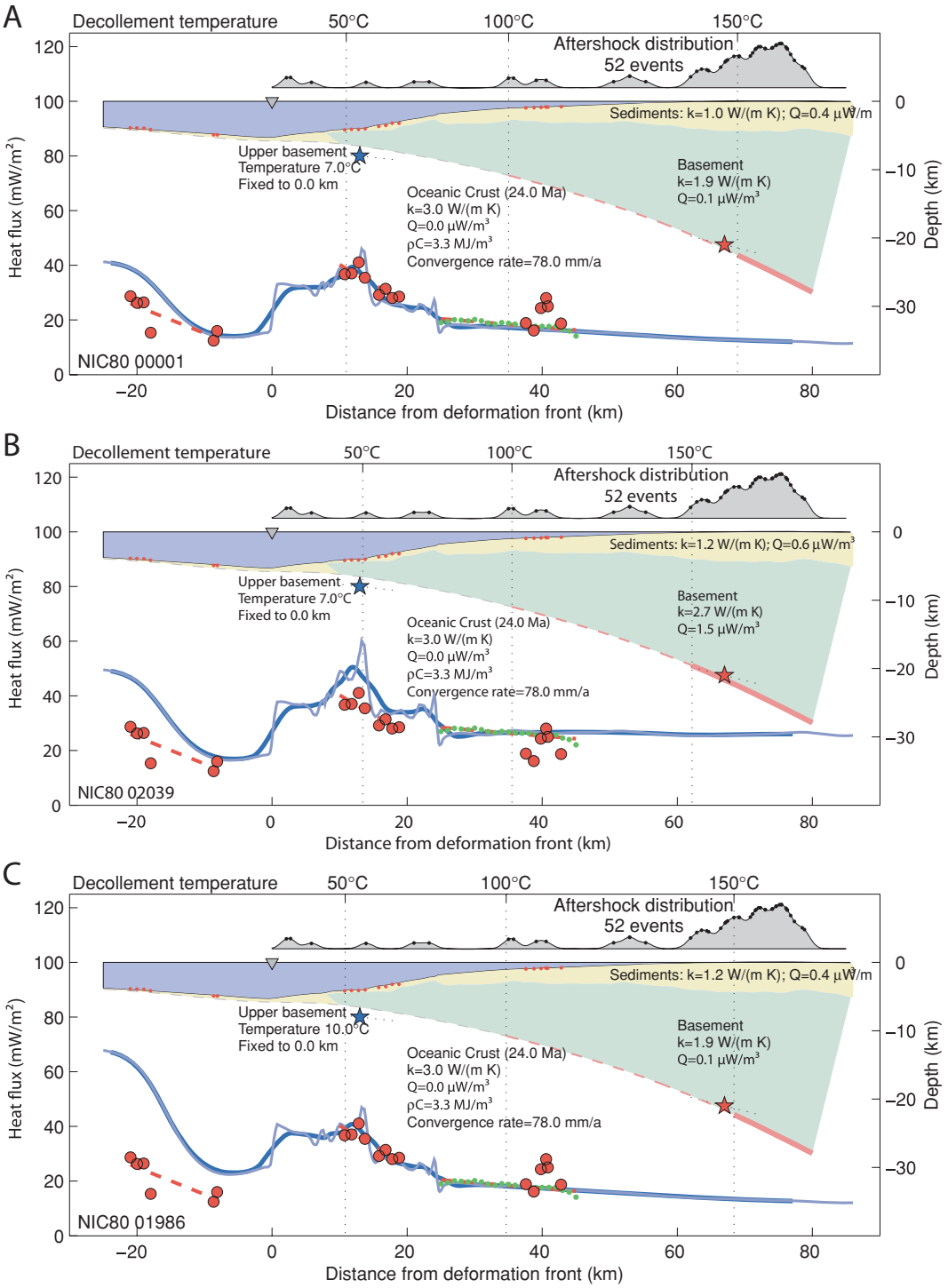

Figure 6. Results from model runs using different sets of parameters used for the three model domains. Smoothed model surface heat-flux values (dark blue line) are compared to measured values (red circles) and estimates from BSR depth (green dots). Locations of the heat-flux measurements with respect to the model geometry are shown as red dots. Black dots and grey area over geometries show aftershock locations projected onto the model transect and their distribution (*cf.* Fig. 1). (a) Initial model based on parameters constrained by parameter observation. (b) Model with parameters chosen by Harris & Wang (2002). (c) Model found by GA, which keeps all parameters in the constrained range and provides a good fit with surface heat-flux data at the same time.

categorized into two distinct groups. Consequently, we considered two calibrations with surface heat-flux values, which represent end-members of the measured data: scenario one based on the lower heat-flux values (6A), and scenario two based on higher values (6B).

Our initial model provides an excellent fit to the first scenario (Fig. 6a), while the model parameters used by Harris & Wang (2002) favour the second scenario (Fig. 6b). The good fit with the initial model and the fact, that the spatially spread out group of lower heat-flux values is more likely to represent an undisturbed

background, whereas the group of higher heat-flux values appears to be a localized anomaly, support the first scenario. Nevertheless, we designed a set of numerical experiments based on a GA to test each scenario and to determine the uncertainties in the modelled temperature distribution on the plate interface.

3.3 Genetic algorithm

The term GA refers to a family of computational codes that are inspired by evolutionary processes. GAs are often used in function optimization, even though the range of possible uses is much broader (Whitley 1994). We chose a GA, because it allows us to find a whole range of optimized solutions while exploring the parameter space in a relatively short period of time. To solve a problem using a GA, a chromosome-like data structure has to be defined which is capable to represent all possible solutions. Then, evolutionary operators are applied to consecutive generations of chromosome sets in order to iteratively increase the overall fitness of the generations. We defined a chromosome as a vector of five floating point numbers containing the variable model parameters, namely the temperature of the upper oceanic crust seawards of the deformation front (T_{in}), the thermal conductivities and heat production rates of the Seds and the CnBs domains. The allowed range for each parameter (*cf.* GA range in Table 1) is intentionally chosen much wider than we expect from the parameter constraints provided above. This allows the GA to test solutions that deviate from our expectations.

The algorithm starts with a random initial generation consisting of 100 chromosomes which is subdivided into 5 populations of 20 chromosomes each (Fig. 7). Consecutively, the fitness of each chromosome is evaluated by the subprocess 'Compute objectives'. The returned objective value depends on the intention with which each of the experiments, described below, is designed. However, the misfit between measured heat-flux data and the heat-flux values computed using the FE model is always a basic component of the objective value. The fit is done using pieces of linear approximations (red dashed lines in Fig. 6) of the measured surface heat-flux data to prevent weighting effects of unevenly distributed data and 'locking' of spikes, present in the modelled data between measured data points. An example for 'locking' being an issue are the heat-flux probe measurements at ∼10 km from the deformation front shown in Fig. 6(a). The subprocess also keeps a record of evaluated chromosomes in order to avoid multiple evaluations of a FEM model with the same set of parameters, since the model runs, lasting ∼30 s each, are demanding most of the computational time.

Choosing parameters controlling the evolutionary operators provided by the GA toolbox for use with Matlab (Chipperfield *et al.* 1994) involves a trade off between fast convergence of the GA with a single possibly locally optimal solution, and a broader exploration of the parameter space. In our experiments, we favoured a broader exploration, since we are interested in the whole range of parameter combinations that solve our problem within the given constraints rather than in a single theoretically best solution.

As shown in Fig. 7, each iteration starts with a ranking of the individual chromosomes which is based on their objective value. Using this ranking, individuals within the different subpopulations of the current generation are selected and recombined to produce a pool of 80 children. Following, some of the generated children are randomly changed by the mutation operator to enhance the genetic diversity. The newly generated children are then rasterized, by rounding, to a discrete parameter grid so that negligible parameter

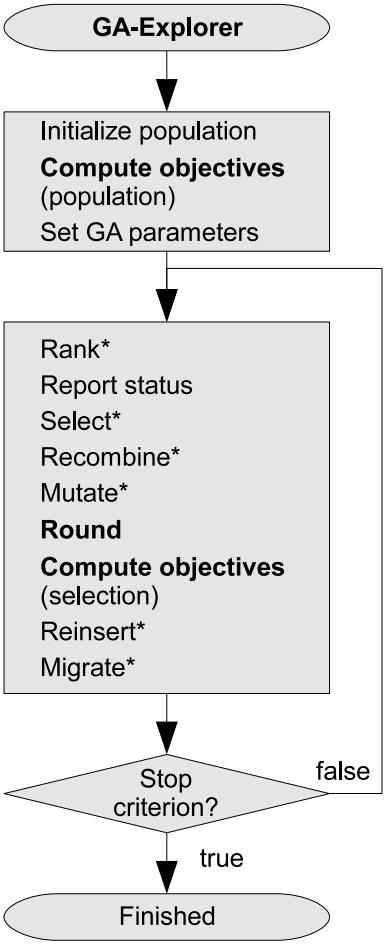

Figure 7. Genetic algorithm used to explore the parameter space of the finite element forward model. Standard evolutionary operators (e.g. Whitley 1994), which are tagged above (*), are based on functions from the genetic algorithm toolbox by Chipperfield *et al.* (1994), while we specifically developed the operators in bold font to reduce the number of forward model evaluations.

variations are mapped onto the same chromosome. After several iterations, this procedure dramatically reduces the number of new FE models that have to be evaluated in each iteration, without loosing a significant amount of information.

Then, a number of children is selected which is reinserted into the parent generation by replacement. Conditionally, some individuals are exchanged between subpopulations by the migration operator in case the generation counter, which is increased with every iteration, reaches predefined levels. Finally, the next iteration step is initiated unless a stop criteria is fulfilled. The stop criteria used by us depend on the amount of computational time has passed, and on the generation diversity. A diversity below a certain threshold indicates that the GA converged against a single solution.

4 NUMERICAL EXPERIMENTS

In a first numerical experiment, we tried to discriminate the two scenarios where the BSR derived heat-flux values are calibrated with the lower or the higher heat-flux probe measurements. To do this, we applied the GA two consecutive times with different objective functions. The two objectives were to minimize the misfit between the modelled surface heat flux and the observed values in respect

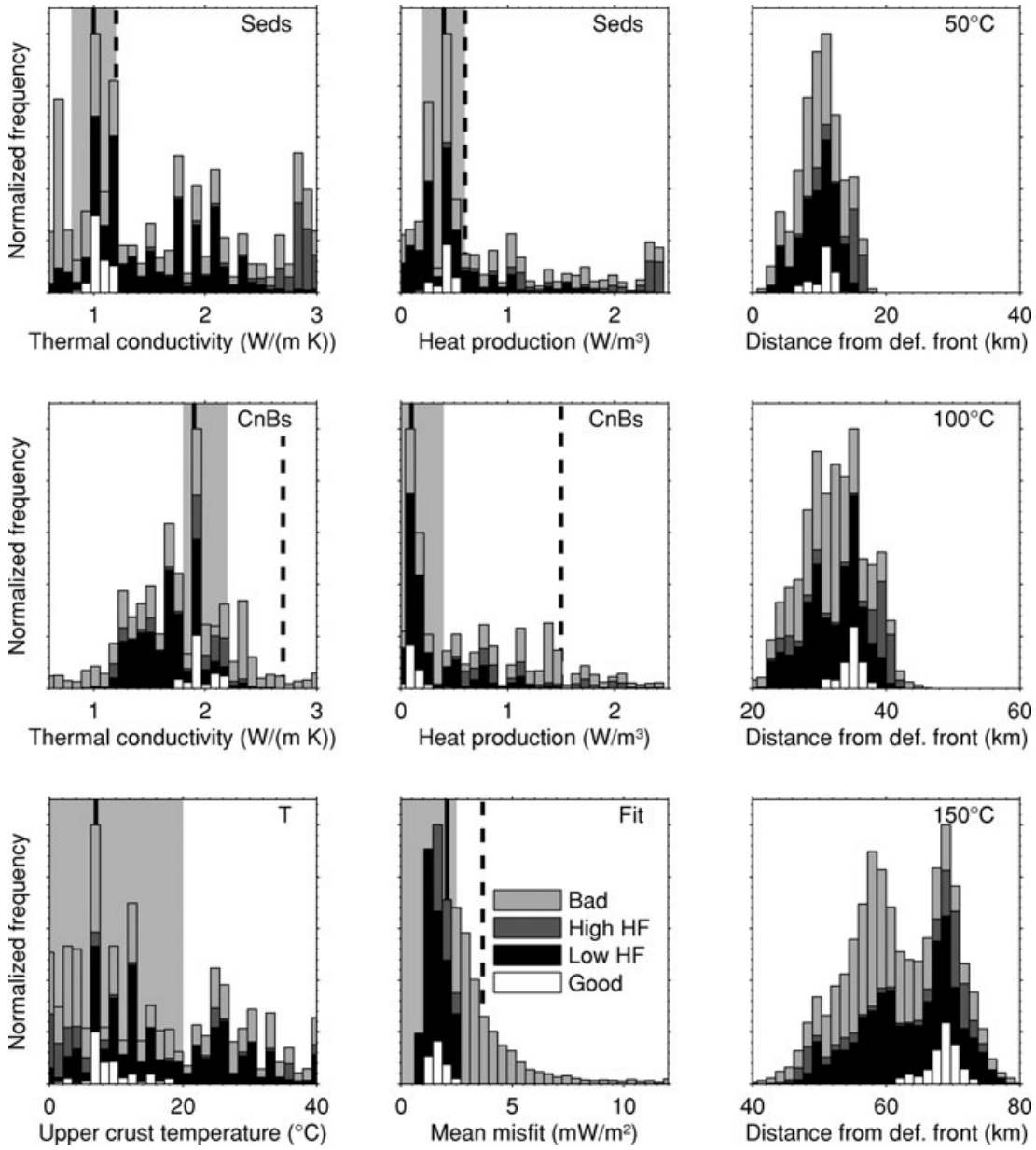

Figure 8. Parameter and result distributions including all 7014 solutions obtained during different numerical experiments. White segments represent good models, which satisfy all constraints highlighted (grey areas) in the six panels of the first two columns. Black and dark grey segments satisfy only the constraint highlighted in the Fit panel in respect to the low and the high heat-flux scenario, respectively. Models that do not meet the Fit criteria are symbolized by light grey segments. The solid vertical line represents the parameters of our initial model, while the dashed lines show the parameters chosen by Harris & Wang (2002).

to the different scenarios. The parameter and result distributions of this and the following numerical experiment are jointly shown in Fig. 8.

Models that represent the low heat-flux scenario are represented by white and black bar segments. Black segments contain models that fit the scenario with a maximum average misfit of 2.5 mW m^{-2} (grey area in the Fit panel), while white bar segments represent the models that additionally fall into the constrained range of all model parameters (highlighted areas in the parameter panels correspond to constraints listed in Table 1). One example for a model that is represented by a white bar segment (good model) is our initial model, which is marked by solid vertical lines in Fig. 8. The solid lines are within the grey areas of all panels. Also the two models that result in smallest and biggest distance of the 150 °C isotherm from the deformation front (listed as deep and shallow in Table 1) while meeting all constraints at the same time are therefore represented by white bar segments.

Having a look at the black segments, it appears that the low heat-flux scenario is satisfied by a wide range of models within the parameter constraints as well as going much beyond them. Actually, the model that provides the best fit to the low heat-flux scenario (*cf.* Table 1) is represented by a black bar segment, since it is based on a very unlikely parameter combination, where the Seds thermal conductivity [1.8 W (m K)$^{-1}$] is higher than of the CnBs [1.6 W (m K)$^{-1}$]. Moreover, it is evident that the low heat-flux scenario is best satisfied by models with low CnBs

thermal conductivities. Values exceeding 2.5 $W\,(m\,K)^{-1}$, expected for regular continental basement, are not conform with the low heat-flux scenario.

Models that meet the high heat-flux scenario within a maximum mean misfit of 2.5 $mW\,m^{-2}$ are symbolized by dark grey bar segments, and models with a misfit exceeding 2.5 $mW\,m^{-2}$ in respect to either heat-flux scenario (i.e. the model represented by the dashed lines, Harris & Wang 2002) are shown as light grey bar segments. Having a look at the dark grey bar segments, it turns out that models satisfying the high heat-flux scenario generally provide a slightly poorer fit to measured data than models that represent the low heat-flux scenario (white and black segments). Moreover, the high heat-flux scenario requires unreasonable Seds thermal conductivities which are greater than 2.5 $W\,(m\,K)^{-1}$. Since there are no known sediments with thermal conductivities exceeding 2.5 $W\,(m\,K)^{-1}$, we reject this scenario.

Having rejected the high heat-flux scenario and verified that models that comply with our parameter constraints are able to reproduce the measured surface heat-flux values, we modified the objective function to study the uncertainty in the model results. To do this, we altered the objective function of the first scenario by adding a penalty for chromosomes containing model parameters that are beyond the range of the parameter constraints. Doing this, more good models, complying with the parameter constraints and fitting the measured heat-flux data at same time (white bar segments), are generated during the iterations of the GA. These additional models provide a good estimate about how much the temperature field along the plate boundary can vary without violating any of the imposed parameter constraints. This is illustrated in the right column of Fig. 8, where the white segments show the possible distances from the deformation front with the 50, 100 and 150 °C isotherms intersecting the plate boundary, respectively. Ranges of these distances are summarized in the constraints row of Table 1. Furthermore, parameters of the models satisfying all parameter constraints and providing the best fit, the shallowest isotherms, and the deepest isotherms are listed. The temperature in the subduction thrust increases from 50 °C ∼10 km landward of the trench axis to 150 °C at ∼20 km depth ∼65 km from the deformation front. As illustrated in Figs 1 and 6, the NEIC hypocentre coincides with the 150 °C isotherm within the given uncertainties.

To study how changes in different parameters effect the modelled results, we computed the Spearman rank correlation coefficients of the relations between the model parameters and the resulting distances of intersection between the 50, 100 and 150 °C isotherms with the plate boundary. The Spearman rank correlation is a non-parametric rank statistic proposed by Spearman in 1904 as a measure of the strength of the associations between two variables (Lehmann & D'Abrera 1975). It assesses how well an arbitrary monotonic function describes the relationship between two variables, without making any assumptions about the frequency distribution of the variables. It does not require the assumption that the relationship between the variables is linear, nor does it require the variables to be measured on interval scales.

The correlation coefficients were computed along with their significance using Matlab® functions implemented by Schloegl (2003). All correlation coefficients, tabulated in Table 2, are significant with a probability of at least 98 per cent. In our model, the temperature of the upper oceanic crust has the strongest correlation with the temperature distribution on the plate boundary, followed by the thermal conductivity off the CnBs and Seds domains. While the correlation of the temperature distribution an the model parameters generally decreases with increasing distance from the deformation front, the correlation with the radiogenic heat production in the CnBs domain is increasingly pronounced.

Table 2. Spearman correlation coefficients of correlation between model parameters and resulting distances of intersection between the 50, 100 and 150 °C isotherms with the plate boundary sorted by magnitude of correlation.

	T_{in}	kCnBS	kSeds	QCnBs	QSeds
$x_{50°C}$	−0.85	0.56	0.48	−0.11	−0.16
$x_{100°C}$	−0.85	0.64	0.40	−0.20	−0.18
$x_{150°C}$	−0.80	0.63	0.38	−0.37	−0.17

5 DISCUSSION AND CONCLUSIONS

We presented a numerical model which is capable of predicting the temperature field at the seismogenic updip limit off Nicaragua, while integrating and satisfying all imposed constraints. We are, however, aware that the relatively simple model cannot fully represent the complex processes that effect an active subduction zone. As is common practice and mentioned earlier, we used 0 °C as a constant value for the bottom water temperature. If the temperatures in the whole model domain were increased by 2 °C to account for the present bottom water temperatures, the 150 °C isotherm would be displaced by about 1 km down slap. Due to the lack of proper constraints, we also had to neglect many other processes with possibly large impact on the thermal state. First, the subduction of sediments was ignored, even though it is known that erosion takes place in the working area (Ranero & von Huene 2000). Furthermore, we did not assign a specific thickness to the cooled layer of the upper oceanic crust as done by Harris & Wang (2002). These effects would lower the temperatures at the décollement, while other processes like frictional heating, which is supposed to be low (Harris & Wang 2002), would increase the temperature. However, adding any of these effects to the model without supplying good constraints would not enhance the performance of the model since all constraints are already satisfied by a whole range of simpler models.

On the other hand, the uncertainty of the model could be reduced by refining the current constraints. Our numerical experiments demonstrated that reliable surface heat-flux measurements provide very useful independent constraints on the model, and the analysis of the correlation coefficients suggest that a refinements of the constraints on the initial thermal state of the subducting oceanic plate and the thermal conductivity of the continental basement have the greatest potential to decrease the uncertainties in the modelled results.

Pelayo & Wiens (1992) investigated several tsunami earthquakes world-wide, including tsunami events in the Kurile trench. It is striking that the 1992 Nicaragua event mimics major features of the 1963 October 20 and 1975 June 10 Kurile tsunami earthquakes. Most important, all three earthquakes were followed by aftershocks arcward and downdip of the main shock. In contrast to this observation, most large interplate earthquakes show aftershocks located seaward of the epicentre, consistent with updip rupture propagation (Kelleher & Sykes 1973). To explain this behaviour, Pelayo & Wiens (1992) suggested that tsunami earthquakes generally nucleate within the typically aseismic region between the updip limit of the seismogenic zone and the trench axis, and that seaward propagation of aftershocks is inhibited by the velocity strengthening behaviour of this zone. In contrast, our results suggest that tsunami earthquakes may nucleate in the uppermost region of the seismogenic zone at temperatures of ∼150 °C.

Faults, like the San Andreas fault, show an upper and lower cut-off of seismicity (Marone & Scholz 1988), indicating that earthquakes only nucleate over a limited depth range in a frictionally unstable region—the seismogenic zone. In subduction zones, the upper transition is defined by the seismic front. Major thrust earthquakes do not nucleate seaward of the seismic front as a consequence of the frictional properties of sediment in the shallow fault zone. In this zone, the plate motion is accommodated by aseismic creep. If earthquakes propagate into this zone of stable sliding, a negative stress drop will occur. This stress drop counteracts and ultimately stops the rupture propagation (Scholz 1998). However, very large earthquakes, that rupture the entire seismogenic zone, can propagate dynamically through the upper stability transition zone and breach the surface (Scholz 1998, 2002). Thus, the main shock of a tsunami earthquake may release enough energy to propagate through this (velocity strengthening) region. In addition, updip propagation could be exacerbated by the presence of elevated fluid pressure that promotes rapid seismic slip at very low frictional resistance (Seno 2002). For Northeast Japan, Tanioka *et al.* (1997) propose an other mechanism. Off Japan, the incoming oceanic lithosphere is highly faulted and exhibits a well-developed horst and graben structure. The same features are observed off Nicaragua (Fig. 1). Though the crust is covered with sediment, horsts and seamounts may breach the sediment blanket and create contact with the hanging wall, which may promote rupture propagation. Consequently, rupture propagation is likely to be governed by the frictional properties of the outcropping basement and the overriding plate, and not by the frictional properties of the sediment. Nevertheless, only very few aftershocks are located in this region (Fig. 1). This suggests that although the rupture could propagate through this area, there is no or little nucleation of events possible seaward of the seismic front. Therefore, using the classification of Scholz (1998, 2002), the region may be characterized by conditionally stable friction behaviour. Modelling fault zones that are only slightly velocity strengthening, Perfettini & Ampuero (2008) showed that sudden stress changes can induce failure with considerable slip acceleration, before the slip rate relaxes back to steady state. From this point of view the 1992 Nicaragua tsunami earthquake might has consisted of a primary earthquake that ruptured the upper part of the seismogenic zone and a secondary event seaward of the updip limit that was triggered by the stress change and was responsible for the large tsunami.

The majority of large and great subduction zone earthquakes nucleate near the downdip limit of the seismogenic zone and propagate updip (Kelleher & Sykes 1973). Such patterns are particularly typical for interface events from the Kuriles, Kamchatka, Aleutians and Mexico (Tichelaar & Ruff 1993) and suggest that confining pressure and temperature have rigidified sediments at depth and caused large and strong contact zones between both plates (Moore *et al.* 2001). During rupture propagation, most subduction thrust earthquakes lose their energy and stop near the updip limit. Tsunami earthquakes, in contrast, tend to nucleate near the updip limit of the coupling zone, where coupling might still be laterally heterogeneous along the thrust contact. In such an environment locked asperities of consolidated and cemented sediment patches are perhaps too small to accumulate stresses required to cause a $M_s > 7$ earthquake. Other processes may therefore contribute to increase normal stress along the plate interface.

Seamount subduction or the subduction of other topographic highs and ridges profoundly affects the state of stress in the subduction thrust. A seamount forced into a subduction zone will increase the normal stress on the subduction interface and hence will enhance seismic coupling (Scholz & Small 1997). Seamounts are indeed abundant on the incoming Cocos plate offshore Nicaragua (Fig. 1). We conclude that in addition to temperature-dependent induration of sediments, increased normal stress by seamount subduction may contribute to accumulate stress sufficient enough to support a $M_s > 7$ earthquake near the updip limit of the seismogenic zone. The resulting energy release may promote dynamic updip rupture propagation through the generally aseismic region seaward of the seismic front.

ACKNOWLEDGMENTS

We are grateful to scientists, master, and crew of RV Meteor cruise M54-2 for having provided support, information and discussion. Special thanks to Norbert Kaul and Bernd Heesemann for assistance during the heat-flow deployments. Moreover, we thank Hugo Perfettini and an anonymous reviewer for their helpful comments. This study was funded by the Deutsche Forschungsgemeinschaft through grant Vi 133/7-1 to University of Bremen and the SFB 574 'Volatiles and fluids in subduction zones' at Christan-Albrechts University, Kiel.

REFERENCES

Baptisa, A1., Priest, G. & Murty, T., 1993. Field survey of the 1992 Nicaragua tsunami, *Mar. Geod.,* **16,** 169–203.

Barckhausen, U., Ranero, C.R., von Huene, R., Cande, S.C. & Roeser, H.A., 2001. Revised tectonic boundaries in the Cocos Plate off Costa Rica: implications for the segmentation of the convergent margin and for plate tectonic models, *J. geophys. Res.,* **106,** 19 207–19 220.

Bilek, S.L. & Lay, T., 2002. Tsunami earthquakes possibly widespread manifestations of frictional conditional stability, *Geophys. Res. Lett.,* **29,** 18–1.

Bookman, C.A., Malone, I. & Langseth, M.G., 1972. Sea floor geothermal measurements from conrad cruise 13, Tech. Rept. 5-CU-5-72, Columbia University, In global heat-fux compilation by Pollack 1991.

Buecker, C. & Rybach, R., 1996. A simple method to determine heat production from gamma-ray logs, *Mar. Petrol. Geol.,* **13,** 373–375.

Byrne, D.E., Davis, D.M. & Sykes, L.R., 1988. Loci and maximum size of thrust earthquakes and the mechanics of the shallow region of subduction zones, *Tectonics,* **7,** 833–857.

Casciola, G. & Romani, L., 2004. A generalized conversion matrix between non-uniform b-spline and bezier representations with applications in CAGD, in *Multivariate Approximation: Theory and Applications*.

Chipperfield, A., Fleming, P.J., Pohlheim, H. & Fonseca, C.M., 1994. Genetic algorithm toolbox for use with matlab, Tech. Rep. 512, Department of Automatic Control and Systems Engineering, University of Sheffield, Version 1.2.

Christensen, D.H. & Ruff, L.J., 1983. Outer-rise earthquakes and seismic coupling, *Geophys. Res. Lett.,* **10,** 697–700.

Comsol, 2005. *Comsol Modeling Guide,* 3rd edn., COMSOL AB, Stockholm.

DeMets, C., 2001. A new estimate for present-day cocos-caribbean plate motion: implications for slip along the central american volcanic arc, *Geophys. Res. Lett.,* **28**(21), 4043–4046.

Divins, D.L., 2005. NGDC total sediment thickness of the world's oceans & marginal seas, Tech. Rep., NGDC.

Geist, E.L., 2002. Complex earthquake rupture and local tsunamis, *J. Geophys. Res. (Solid Earth),* **107,** 2–1.

Geist, E.L. & Bilek, S.L., 2001. Effect of depth-dependent shear modulus on tsunami generation along subduction zones, *Geophys. Res. Lett.,* **28**(7), 1315–1318.

Geist, E.L., Bilek, S.L., Arcas, D. & Titov, V.V., 2006. Differences in tsunami generation between the december 26, 2004 and march 28, 2005 sumatra earthquakes, *Earth Planets Space,* **58**(2), 185–193.

Grevemeyer, I. & Villinger, H., 2001. Gas hydrate stability and the assessment of heat flow through continental margins, *Geophys. J. Int.,* **145**(3), 647–660.

Grevemeyer, I., Diaz-Naveas, J.L., Ranero, C.R. & Villinger, H.W., 2003. Heat flow over the descending Nazca plate in central chile, 32[deg]s to 41[deg]s: observations from ODP leg 202 and the occurrence of natural gas hydrates, *Earth planet. Sci. Lett.,* **213**(3-4), 285–298.

Grevemeyer, I., Kaul, N., Diaz-Naveas, J.L., Villinger, H.W., Ranero, C.R. & Reichert, C., 2005. Heat flow and bending-related faulting at subduction trenches: case studies offshore of nicaragua and central chile, *Earth planet. Sci. Lett.,* **236**(1-2), 238–248.

Harris, R.N. & Wang, K., 2002. Thermal models of the Middle America Trench at the Nicoya Peninsula, Costa Rica, *Geophys. Res. Lett.,* **29,** 6–1.

Hartmann, A. & Villinger, H., 2002. Inversion of marine heat flow measurements by expansion of the temperature decay function, *Geophys. J. Int.,* **148**(3), 628–636.

Hyndman, R.D. & Wang, K., 1993. Thermal constraints on the zone of major thrust earthquake failure—the cascadia subduction zone, *J. geopyhs. Res.,* **98,** 2039–2060.

Hyndman, R.D., Davis, E.E. & Wright, J.A., 1979. The measurement of marine geothermal heat flow by a multipenetration probe with digital acoustic telemetry and insitu thermal conductivity, *Mar. Geophys. Res.,* **4**(2), 181–205.

Hyndman, R.D., Wang, K. & Yamano, M., 1995. Thermal constraints on the seismogenic portion of the southwestern Japan subduction thrust, *J. geophys. Res.,* **100,** 15 373–15 392.

Ide, S., Imamura, F., Yoshida, Y. & Abe, K., 1993. Source characteristics of the Nicaraguan tsunami earthquake of September 2, 1992, *Geophys. Res. Lett.,* **20,** 863–866.

Ihmle, P.F., 1996a. Frequency-dependent relocation of the 1992 nicaragua slow earthquake: an empirical Green's function approach, *Geophys. J. Int.,* **127**(1), 75–85.

Ihmle, P.F., 1996b. Monte Carlo slip inversion in the frequency domain: application to the 1992 Nicaragua slow earthquake, *Geophys. Res. Lett.,* **23,** 913–916.

Kanamori, H., 1972. Mechanism of tsunami earthquakes, *Phys. Earth planet. Int.,* **6,** 346–359.

Kanamori, H. & Kikuchi, M., 1993. The 1992 nicaragua earthquake: a slow tsunami earthquake associated with subducted sediments, *Nature,* **361**(6414), 714–716.

Kelleher, J.L. & Sykes, J.O., 1973. Possible criteria for predicting earthquake locations and their applications to major plate boundaries of the pacific and caribbean, *J. geophys. Res.,* **78,** 2547–22585.

Kimura, G., Silver, E., Blum, P. & Shipboard Scientific Party, 1997. Init. repts., in *Proc. ODP,*vol. 170, College Station, TX (Ocean Drilling Program).

Langseth, M.G. & Silver, E.A., 1996. The Nicoya convergent margin-a region of exceptionally low heat flow, *Geophys. Res. Lett.,* **23**(8), 891–894.

Langseth, M.G., Malone, I. & Berger, D., 1971. Sea floor geothermal measurements from vema cruise 24, Tech. Rept. 3-CU-3-71, Columbia University, In global heat-fux compilation by Pollack 1991.

Lehmann, E.L. & D'Abrera, H.J.M., 1975. *Nonparametrics: Statistical Methods Based on Ranks*, Prentice-Hall, Upper Saddle River, NJ.

Marone, C. & Scholz, C.H., 1988. The depth of seismic faulting and the upper transition from stable to unstable slip regimes, *Geophys. Res. Lett.,* **15,** 621–624.

Mayer, L., Pisias, N., Janecek, T. & Shipboard Scientific Party, 1992. Init. repts., in *Proc. ODP,* no. 138, College Station, TX (Ocean Drilling Program).

Moore, G.F., Taira, A., Klaus, A. & Shipboard Scientific Party, 2001. Init. repts., in *Proc. ODP,*vol. 190 [Online], Available from World Wide Web:http://www-odp.tamu.edu/publications/190_IR/190ir.htm.

Moore, J.C. & Saffer, D., 2001. Updip limit of the seismogenic zone beneath the accretionary prism of Southwest Japan: an effect of diagenetic to low-grade metamorphic processes and increasing effective stress, *Geology,* **29**(2), 183–186.

Morris, J.D., Villinger, H.W., Klaus, A. & Shipboard Scientific Party, 2003. Init. repts., in *Proc. ODP,* **vol. 205** [Online], Available from World Wide Web:http://www-odp.tamu.edu/publications/205_IR/205ir.htm.

Newman, A.V., Schwartz, S.Y., Gonzalez, V., DeShon, H.R., Protti, J.M. & Dorman, L.M., 2002. Along-strike variability in the seismogenic zone below Nicoya Peninsula, Costa Rica, *Geophys. Res. Lett.,* **29,** 38–1.

NGDC, 2005. Global digital elevation model (ETOPO2), National Geophysical Data Center.

Nielsen, H.B., 2005. *Immoptibox: A Matlab Toolbox for Optimization and Data Fitting,* Informatics and Mathematical Modelling, Technical University of Denmark.

Oleskevich, D.A., Hyndman, R.D. & Wang, K., 1999. The updip and downdip limits to great subduction earthquakes: thermal and structural models of Cascadia, South Alaska, SW Japan, and Chile, *J. geophys. Res.,* **104,** 14 965–14 992.

Pelayo, A.M. & Wiens, D.A., 1992. Tsunami earthquakes-slow thrust-faulting events in the accretionary wedge, *J. geophys. Res.,* **97**(B11), 15 321–15 337.

Perfettini, H. & Ampuero, J.-P., 2008. Dynamics of a velocity strengthening fault region: implications for slow earthquakes and postseismic slip, *J. geophys. Res.,* **113**, B09411.

Pfender, M. & Villinger, H., 2002. Miniaturized data loggers for deep sea sediment temperature gradient measurements, *Mar. Geol.,* **186,** 557–570.

Polet, J. & Kanamori, H., 2000. Shallow subduction zone earthquakes and their tsunamigenic potential, *Geophys. J. Int.,* **142,** 684–702.

Pollack, H.N., Hurter, S.J. & Johnston, J.R., 1992. Global heat flow data set, Tech. rep., World Data Center A for Solid Earth Geophysics, NOAA E/GCI, 325 Broadway, Boulder, CO 80303, USA.

Ranero, C.R. & von Huene, R., 2000. Subduction erosion along the Middle America convergent margin, *Nature,* **404,** 748–752.

Ranero, C.R., von Huene, R., Flueh, E., Duarte, M., Baca, D. & McIntosh, K., 2000. A cross section of the convergent Pacific margin of Nicaragua, *Tectonics,* **19,** 335–357.

Romani, L. & Sabin, M.A., 2004. The conversion matrix between uniform B-spline and Bézier representations, *Comput. Aided Geom. Des.,* **21,** 549–560.

Satake, K., 1994. Mechanics of the 1992 Nicaragua tsunami earthquake, *Geophys. Res. Lett.,* **21,** 2519–2522.

Satake, K. & Tanioka, Y., 1999. Sources of tsunami and tsunamigenic earthquakes in subduction zones, *Pure appl. Geophys.,* **V154**(3), 467–483.

Satake, K. *et al.*, 1993. Tsunami field survey of the 1992 nicaragua earthquake, *EOS Transactions,* **74,** 145–145.

Schloegl, A., 2003. *The NaN-Toolbox: A Statistic-Toolbox for Octave and Matlab,* Version 1.52.

Scholz, C.H., 1998. Earthquakes and friction laws, *Nature,* **391**(6662), 37–42.

Scholz, C.H., 2002. *The Mechanics of Earthquakes and Faulting,* Cambridge Univ. Press, Cambridge.

Scholz, C.H. & Small, C., 1997. The effect of seamount subduction on seismic coupling, *Geology,* **25**(6), 487–490.

Sclater, J.G., G., R.U. & Dixon, F.S., 1970. Heat flow in the southwestern pacific, *J. geophys. Res.,* **75,** 333–348, In global heat-fux compilation by Pollack 1991.

Seno, T., 2002. Tsunami earthquakes as transient phenomena, *Geophys. Res. Lett.,* **29**(10), 1419.

Stein, C.A. & Stein, S., 1992. A model for the global variation in oceanic depth and heat flow with lithospheric age, *Nature,* **359**(6391), 123–129.

Tanioka, Y., Ruff, L. & Satake, K., 1997. What controls the lateral variation of large earthquake occurrence along the japan trench, *The Island Arc,* **6,** 261–266.

Tichelaar, B.W. & Ruff, L.J., 1993. Depth of seismic coupling along subduction zones, *J. geophys. Res.,* **98,** 2017–2037.

UNAVCO, 2006. Plate motion calculator.

Vaquier, V., Sclater, J.G. & Corry, C.E., 1967. Studies of the thermal state of the earth, the 21st paper-heat flow, eastern pacific, *Bull. Earthq. Res. Inst.*

Tokyo Univ.], **45,** 375–393, In global heat-fux compilation by Pollack 1991.

Velasco, A.A., Ammon, C.J., Lay, T. & Zhang, J., 1994. Imaging a slow bilateral rupture with broadband seismic waves: the September 2, 1992 Nicaraguan tsunami earthquake, *Geophys. Res. Lett.,* **21,** 2629–2632.

von Herzen, R. & Maxwell, M.E., 1959. The measurement of thermal conductivity of deep sea sediments by a needle probe method, *J. geophys. Res.,* **64,** 1557–1563.

Walther, C.H.E., Flueh, E.R., Ranero, C.R., von Huene, R. & Strauch, W., 2000. Crustal structure across the pacific margin of nicaragua:evidence for Ophiolitic basement and a shallow mantle sliver, *Geophys. J. Int.,* **141,** 759–777.

Whitley, D., 1994. A genetic algorithm tutorial, *Stat. Comput.,* **4,** 65–85.

Wilson, D., Teagle, D., Acton, G. & Shipboard Scientific Party, 2003. Init. repts., in *Proc. ODP,* no. 206, College Station, TX (Ocean Drilling Program).